

A Novel Miniaturized Image Rejection Bandpass Filter Basing on Stepped-Impedance Resonators

Guangxiu Zhao¹, Chen Li¹, Minquan Li^{1, *}, Pingjuan Zhang²,
Yajin Yan¹, Xiaming Mo¹, and Ziyun Tu¹

Abstract—In order to meet the requirements for the suppression of mirror frequencies in the 5G RF front end, this paper proposes a novel miniaturized image rejection bandpass filter by loading Stepped-Impedance Resonators (SIR). By analyzing the relationship between the impedance ratio of a half-wavelength SIR and its electrical length, we have designed an improved second-order bandpass filter, which reduces the size by 34.3% compared to traditional five-order hairpin filters. In order to further enhance the performance of the filter, the use of a radial stub, as opposed to the traditional rectangular open stub, allows for the generation of a wider band transmission zero, which can be analyzed using lumped equivalent circuits. This integration improves the stopband rejection of the filter. The results show that the passband range is 5.35 GHz–6.64 GHz; the rejection in the stopband range 8.10 GHz–11.98 GHz is over 45 dB; and the size is only $0.385\lambda_g \times 0.295\lambda_g$.

1. INTRODUCTION

The existing WiFi6 network primarily operates in the 2.4 GHz and 5 GHz frequency bands. However, due to the increasing demand for high transmission rates and wideband applications, as well as the congestion in the existing wireless spectrum, a new frequency range has been added from 5.925 GHz to 6.425 GHz, known as WiFi6E [1–3]. In WiFi6E equipment, which utilizes the frequency band deployment from UNII-2C to UNII-5, the use of a superheterodyne structure receiver with a local oscillator frequency set at 8.07 GHz results in an image frequency range of 10.67 GHz to 11.625 GHz. To minimize the noise interference from the image frequency, a receiver employing this architecture typically requires an Image Rejection Ratio (IRR) above 30 dB [4].

While waveguide filters offer low insertion loss, high selectivity, and excellent stopband rejection, they are not suitable for miniaturized devices due to their large size. In [5], a wideband bandpass filter is established by etching a square Complementary Split Ring Resonator (CSRR) structure in the middle layer of Folded Substrate Integrated Waveguide (FSIW). The innovation of this structure lies in its ability to maintain the integrity of the planar surface, allowing seamless integration with other planar circuits. However, the filter's size remains relatively large. On the other hand, Bulk Acoustic Wave (BAW) filters can provide a more compact size, but achieving wide bandwidth on specific piezoelectric materials becomes challenging. Moreover, BAW filters struggle to simultaneously address bandwidth, stopband rejection, insertion loss, and physical size requirements. In [6], a bandpass filter based on AlScN piezoelectric thin films for WiFi6/6E/7 applications is proposed. It exhibits superior system efficiency within the UN II 1–8 frequency range, but its skirt selectivity is not optimal. In [7], a new generation BAW technology covering the 1–8 GHz range is introduced. Although it significantly optimizes the quality factor Q and reduces the filter size, the insertion loss issue remains to be addressed.

Received 30 June 2023, Accepted 9 August 2023, Scheduled 19 August 2023

* Corresponding author: Minquan Li (AHU411MHz@hotmail.com).

¹ Key Lab of Ministry of Education of Intelligent Computing & Signal Processing, Anhui University, Hefei 230601, China. ² Anhui Science and Technology University, Bengbu 233100, China.

In [8, 9], the use of different piezoelectric thin films in a BAW/SAW (Surface Acoustic Wave) hybrid structure demonstrates a noticeable improvement in coupling efficiency. However, similar to the previous cases, both configurations still suffer from poor insertion loss performance. In contrast, the microstrip structure, widely employed in filter design, offers various resonator structures that can be tailored according to different application. In [10], a wideband bandpass filter based on a Π -shaped cross-section structure is proposed. This structure can be applied to various planar topologies, achieving excellent performance in terms of wide bandwidth, miniaturization, and low insertion loss. To suppress spurious frequencies in the bandpass filter, a miniaturized wide stopband filter with more than 20 dB attenuation at 15 times of the center frequency is achieved by using half-wavelength and quarter-wavelength Uniform Impedance Resonator (UIR) resonators [11]. A microstrip bandpass filter designed for the WLAN frequency range combines U-shaped resonators with Defected Ground Structure (DGS) to achieve its characteristics [12]. In [13], to suppress third harmonic distortion, two SIR (Stepped Impedance Resonator) resonators are utilized and arranged in reverse to form a wideband response. For the implementation of two 5G low-frequency bandpass filters in both filtering and reconfigurable antenna projects, hairpin bandpass filters are proposed in [14], with good results in terms of return loss and insertion loss performance. However, achieving higher and wider stopband rejection with fewer resonator orders to attain an IRR higher than 30 dB remains a challenge.

This paper introduces a novel design method for a compact image rejection filter operating in the 5.5 GHz to 6.5 GHz frequency range. The proposed method aims to achieve low insertion loss while maintaining high stopband rejection in the frequency range of 10.67 GHz to 11.625 GHz. By addressing these design challenges, the proposed approach holds promise for enhancing the performance of WiFi6E receivers in terms of image rejection and overall system efficiency.

2. FILTER DESIGN

2.1. Miniaturized Filter Design

SIR encompasses three fundamental structures: $\lambda_g/4$, $\lambda_g/2$, and λ_g . Figure 1 illustrates a $\lambda_g/2$ SIR structure. The resonator consists of three sections: two microstrip lines on either side with an impedance of Z_2 and an electrical length of θ_2 , and a middle microstrip line with an impedance of Z_1 and an electrical length of $2\theta_1$. The total electrical length of the resonator is denoted as θ_t , and the impedance ratio is defined as $k = Z_2/Z_1$. The transmission matrix and input admittance of the $\lambda_g/2$ SIR structure depicted in Figure 1 are represented by Equations (1) and (2):

$$\begin{bmatrix} A & B \\ C & D \end{bmatrix} = \begin{bmatrix} \cos \theta_2 & jZ_2 \sin \theta_2 \\ j \sin \theta_2 / Z_2 & \cos \theta_2 \end{bmatrix} \begin{bmatrix} \cos 2\theta_1 & jZ_1 \sin 2\theta_1 \\ j \sin 2\theta_1 / Z_1 & \cos 2\theta_1 \end{bmatrix} \begin{bmatrix} \cos \theta_2 & jZ_2 \sin \theta_2 \\ j \sin \theta_2 / Z_2 & \cos \theta_2 \end{bmatrix} \quad (1)$$

$$Y_{in} = \frac{C}{A} = jY_2 \frac{2(k \tan \theta_1 + \tan \theta_2) \cdot (k - \tan \theta_1 \tan \theta_2)}{k(1 - \tan^2 \theta_1)(1 - \tan^2 \theta_2) - 2(1 - k^2) \cdot \tan \theta_1 \cdot \tan \theta_2} \quad (2)$$

When $Y_{in} = 0$, the resonance condition can be obtained as:

$$\tan \theta_1 \tan \theta_2 = k \quad (3)$$

Since the total length of the resonator θ_t can be expressed as $\theta_t = 2\theta_1 + 2\theta_2$, it can be substituted into Equation (3) for calculation:

$$\theta_t = 2 \arctan \frac{k + \tan^2 \theta_1}{(1 - k) \tan \theta_1} \quad (4)$$

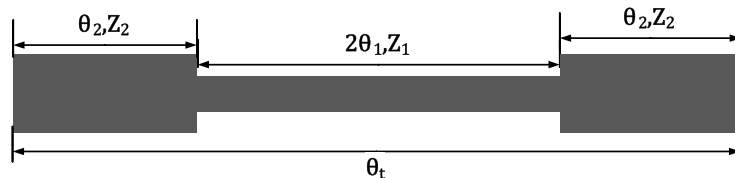


Figure 1. Half-wavelength SIR structure.

From the above equation, we can understand that the total electrical length θ_t of the half-wavelength SIR is not only determined by θ_1 but also related to the impedance ratio k . Figure 2 shows the curve of θ_t varying with θ_1 for different values of k . From Figure 2, it can be observed that when the impedance ratio $k < 1$, the total electrical length θ_t of the half-wavelength SIR reaches its minimum value. This indicates that the total electrical length of the SIR is smaller when the impedance ratio is less than 1 than that using a Uniform Impedance Resonator (UIR). Consequently, this characteristic can be leveraged to facilitate the design of miniaturized filters. When $k = 1$, the resonator becomes a UIR. When $k > 1$, θ_t reaches its maximum value, indicating that the resonator's electrical size is larger than that of a UIR.

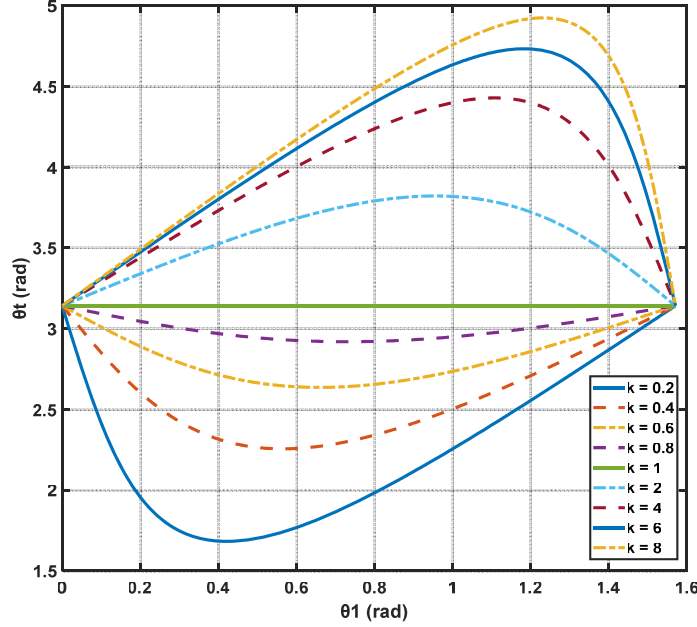


Figure 2. The curve graph of θ_1 varying with θ_t under different impedance ratios.

Let's denote the fundamental frequency and each spurious frequency as f_{sn} ($n = 0, 1, 2, 3\dots$), and set $Y_{in} = 0$ to obtain the values of f_{sn} . We can analyze the ratio of each spurious frequency to the fundamental frequency. For ease of calculation, let $\theta_1 = \theta_2 = \theta_0$, and the input admittance can be simplified as follows.

$$Y_{in} = jY_2 \frac{2(k+1) \tan \theta_0 \cdot (k - \tan^2 \theta_0^2)}{k(1 - \tan^2 \theta_0)^2 - 2(1 - k^2) \cdot \tan^2 \theta_0} \quad (5)$$

By setting the input admittance Y_{in} to 0, we can obtain the following:

$$\theta_0 = \arctan \sqrt{k} \quad (6)$$

$$\theta_{s1} = \pi/2 \quad (7)$$

$$\theta_{s2} = \pi - \arctan \sqrt{k} \quad (8)$$

$$\theta_{s3} = \pi \quad (9)$$

Then it can be deduced that the ratio of each parasitic frequency to the fundamental frequency is:

$$\frac{f_{s1}}{f_0} = \frac{\theta_{s1}}{\theta_0} = \frac{\pi}{2 \arctan \sqrt{k}} \quad (10)$$

$$\frac{f_{s2}}{f_0} = \frac{\theta_{s2}}{\theta_0} = \frac{\pi - \arctan \sqrt{k}}{\arctan \sqrt{k}} \quad (11)$$

$$\frac{f_{s3}}{f_0} = \frac{\theta_{s3}}{\theta_0} = \frac{\pi}{\arctan \sqrt{k}} \quad (12)$$

Equations (10), (11), and (12) reveal that the spurious frequency is influenced by the impedance ratio k . By manipulating the value of k , the fundamental frequency and spurious frequency can be adjusted accordingly. This characteristic can be effectively utilized for achieving a wide stopband design in filters.

In order to validate the aforementioned theory, a 5th-order traditional hairpin filter is designed with a center frequency of $f_0 = 6$ GHz, bandwidth of $BW = 1.0$ GHz, insertion loss of $IL < 1$ dB, and $IRR > 30$ dB. The structure of the filter is depicted in Figure 3. To reduce the size of the filter, a SIR is introduced. As shown in Figure 4(a), the improved filter exhibits a more compact size with a relative reduction of 34.3%. Figure 4(b) compares the simulated S_{21} and S_{11} data of the traditional hairpin filter and the improved second-order hairpin filter. It can be observed that the improved second-order hairpin filter demonstrates improvements in terms of center frequency, relative bandwidth, insertion loss, and return loss. However, the stopband rejection is slightly reduced. Therefore, in Section 2.2, our focus will be on enhancing the filter design in terms of stopband rejection, particularly in the upper stopband.



Figure 3. Layout of conventional fifth-order BPF.

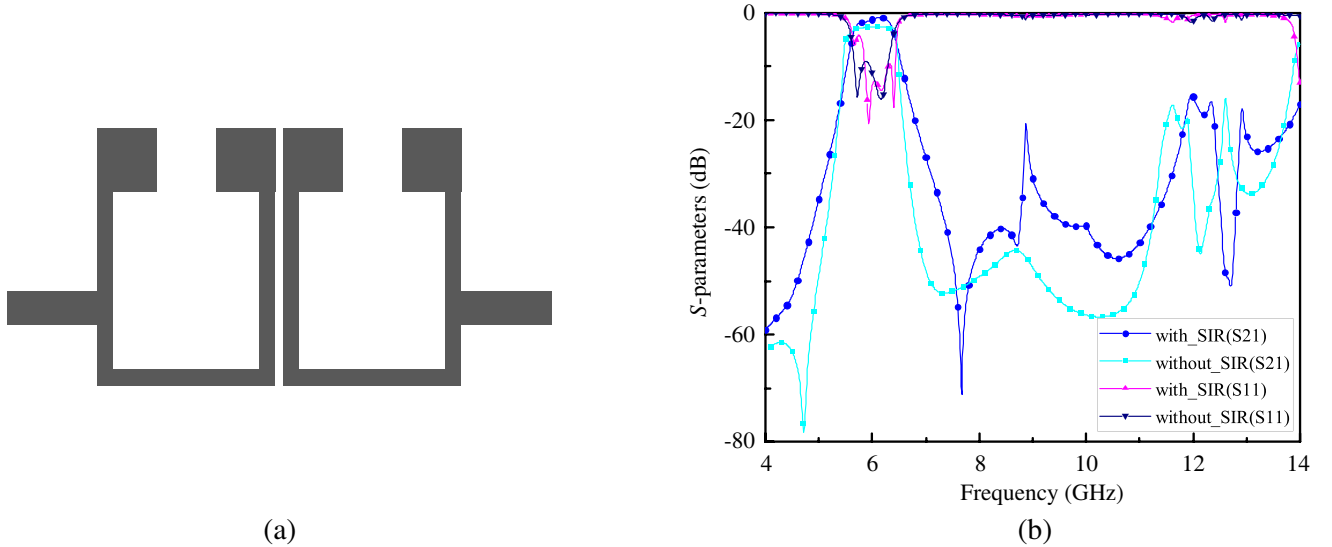


Figure 4. Second-order SIR hairpin filter. (a) Layout of second-order BPF. (b) Comparison of S -parameters between the traditional and second-order SIR hairpin filters.

2.2. Miniaturized and High Image Rejection Filter Design

Radial stubs are commonly utilized to introduce additional transmission zeros, as depicted in Figure 5(a). In this structure, the angle is defined as θ , the inner radius as ds , the outer radius as r , the relative permittivity of the dielectric substrate as ϵ_r , and the thickness as h . As shown in Figure 5(b), the radial stub can be equivalently represented as an LC series circuit. This structure can

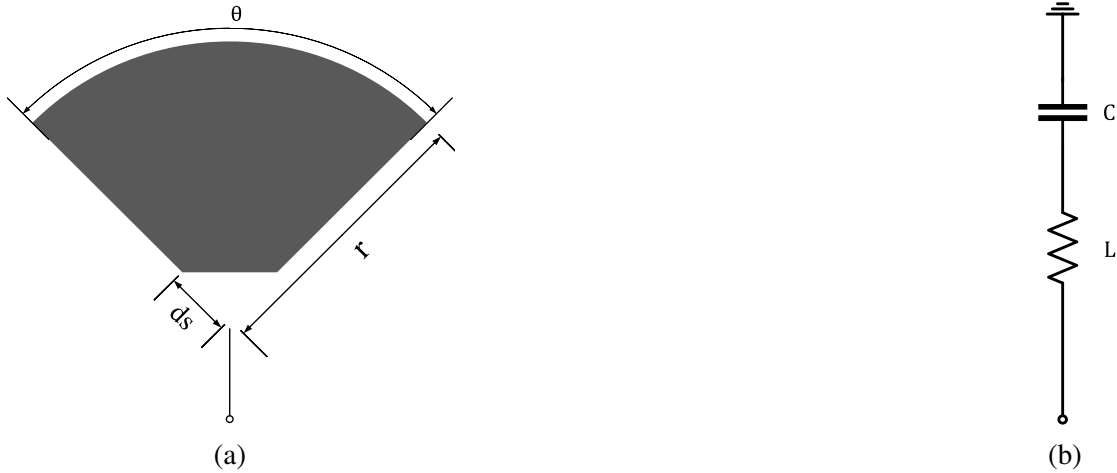


Figure 5. (a) Radial stub. (b) Radial stub equivalent lumped circuit.

be connected in parallel within the circuit, resulting in resonance at a specific frequency and generating a transmission zero.

As introduced in [15], the capacitance C and inductance L of the lumped element equivalent to the radial stub are:

$$C = \frac{r\sqrt{8\epsilon_{eff}}}{Z_c c \cos(\theta/2)} \tag{13}$$

$$L = \frac{1}{c\omega_0^2} = \frac{Z_c r\sqrt{8\epsilon_{eff}}}{\pi^2 c \cos(\theta/2)} \tag{14}$$

Equations (11) and (12) demonstrate the relationship between the equivalent capacitance and equivalent inductance of the radial stub’s LC circuit and its outer diameter r , inner diameter ds , and angle θ . To examine the impact of the radial stub’s outer diameter r on the equivalent capacitance and inductance, the radial equivalent circuit is extracted using ADS software. A $50\ \Omega$ microstrip line is connected in parallel to a radial stub with $ds = 0.7\ \text{mm}$ and $\theta = 90$ on a Rogers 4350B dielectric substrate with a thickness of $0.508\ \text{mm}$ and a dielectric constant of 3.66 . The equivalent circuit is then extracted for three different outer diameters: $r = 4.7\ \text{mm}$, $r = 4.9\ \text{mm}$, and $r = 5.1\ \text{mm}$. The extracted equivalent circuit parameters are presented in Table 1. Figure 6 shows the simulated S -parameters of the radial stubs with different outer diameters.

Table 1. Extracted equivalent circuit parameters.

Parameters	$r = 4.7\ \text{mm}$	$r = 4.9\ \text{mm}$	$r = 5.1\ \text{mm}$
C (pF)	1.73	1.88	2.07
L (nH)	0.41	0.41	0.41
f_0 (GHz)	6.249	5.996	5.724

To further enhance the stopband rejection performance of the second-order SIR hairpin filter, the previously mentioned radial stub is paralleled to the middle section of the second-order SIR filter resonator depicted in Figure 4(a). This modified filter structure is presented in Figure 7(a). The radial stub dimensions are as follows: $ds = 0.7\ \text{mm}$, $\theta = 75^\circ$, $r = 4.2\ \text{mm}$, with an equivalent capacitance of $C = 1.32\ \text{pF}$ and an equivalent inductance of $L = 0.36\ \text{nH}$. The resonance frequency is set at $f_0 = 8.01\ \text{GHz}$. Due to the introduction of the stub, slight adjustments are made to the physical dimensions of the middle section of the resonator to ensure compatibility with the original

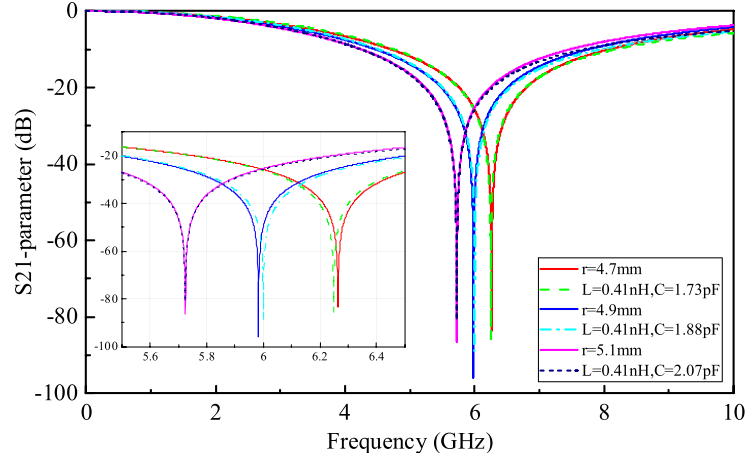


Figure 6. Comparison of distributed parameters and lumped parameters equivalent circuit simulation of radial stubs.

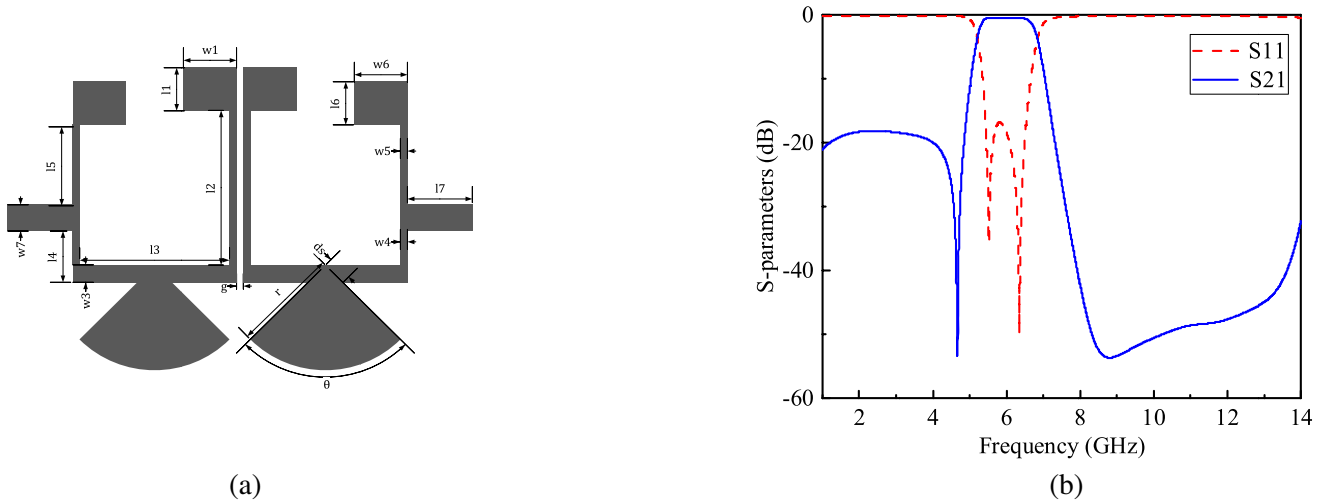
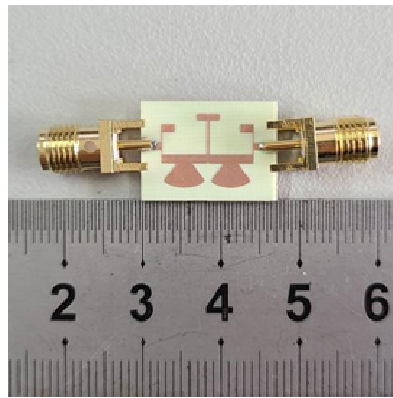


Figure 7. (a) Layout of a second-order SIR hairpin filter loaded with radial stubs. (b) Simulation results.

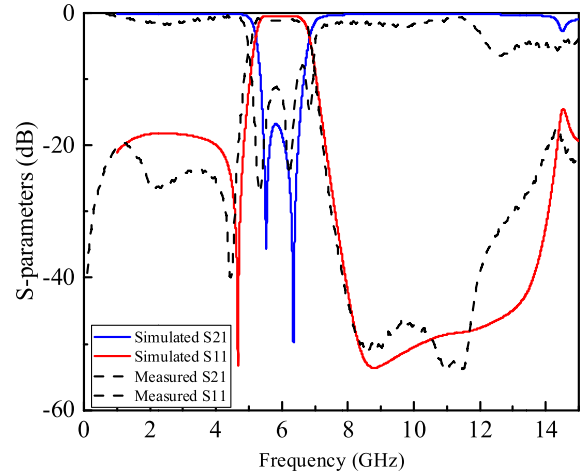
passband. Consequently, a compact wide stopband filter with high stopband rejection is designed, while maintaining consistency with the original passband. The simulation results are illustrated in Figure 7(b). The final optimized values are: $w1 = 1.4$ mm, $w2 = 0.1$ mm, $w3 = 0.9$ mm, $w5 = 0.1$ mm, $w6 = 1.7$ mm, $w7 = 0.8$ mm, $l1 = 0.8$ mm, $l2 = 4.4$ mm, $l3 = 5.5$ mm, $l4 = 1.6$ mm, $l5 = 0.4$ mm, $l6 = 1$ mm, $l7 = 3$ mm, $r = 4.2$ mm, $ds = 0.7$ mm, $\theta = 75^\circ$, $g = 0.1$ mm.

3. MEASUREMENT AND ANALYSIS

To validate the proposed design method, the designed filter is simulated, fabricated, and tested. The fabricated filter is shown in Figure 8(a), while the comparison between the measured and simulated results is shown in Figure 8(b). Analyzing Figure 8(b), it is evident that the measured passband frequency range spans from 5.35 GHz to 6.64 GHz, exhibiting a relative bandwidth of 21.5%. The insertion loss remains below 1.12 dB, and exceptional stopband rejection surpasses 45 dB within 8.12 GHz to 11.98 GHz frequency range. Remarkably, the compact size of the fabricated filter measures merely 11.5 mm \times 8.8 mm, signifying an 83.22% reduction in size compared to the traditional fifth-order hairpin filter. The measurement results are in good agreement with the simulation ones, thus affirming the accuracy of the proposed design methodology. This novel bandpass filter, in comparison to prior



(a)



(b)

Figure 8. (a) Fabricated filter. (b) Simulated and measured S_{11} and S_{21} S -parameters of the filter.

counterparts, demonstrates superior stopband rejection capabilities and a significantly compact form factor. Table 2 provides a comprehensive comparison between the bandpass filter proposed in this paper and other filters of similar type.

Table 2. Comparison of proposed filter with similar bandpass filters.

Reference	f_0 (GHz)	IL (dB)	3 dB FBW (%)	Rejection (dB)	Size ($\lambda_g \times \lambda_g$)
[5]	5.87	1.2	35.5	20@7.2 GHz–8.9 GHz	1.022×0.513
[12]	5.8	1.8	4.1	30@6.3 GHz–8.0 GHz	1.06×0.156
[13]	4.2	1.2	55	15@7.5 GHz–12.0 GHz	0.3×0.1
[14]	6.61	1.17	30	15@8.3 GHz–10.8 GHz	0.66×0.27
This Work	6.0	1.12	22	45@8.10 GHz–11.98 GHz	0.385×0.295

4. CONCLUSION

This paper proposes a novel microstrip image rejection bandpass filter, effectively reducing the size of the resonator and the order of the filter by replacing the traditional hairpin filter’s Uniform Impedance Resonator (UIR) structure with a half-wavelength Stepped Impedance Resonator (SIR) structure, thereby successfully achieving miniaturization of the filter. Additionally, by introducing a radial stub in the upper stopband to create a controllable transmission zero, the filter achieves attenuation greater than 45 dB within the range of 8.10 GHz to 11.98 GHz. Compared to the traditional hairpin filter, the designed filter’s physical size is reduced by 83.22%. The measured results highly match the simulation ones, confirming the filter’s characteristics of miniaturization, high stopband rejection, and low insertion loss. Therefore, this design method can be widely applied to the design of image rejection filters for the 5G RF front-end.

ACKNOWLEDGMENT

This work is supported by the Key Natural Science Research Project of Anhui Higher Education Institutions: Research and application on electromagnetic regulation mechanism of artificial magnetic conductor materials 2022AH050070, and the National Nature Science Foundation of China 62101002, U22A2017, U20A20164.

REFERENCES

1. Oughton, E. J., W. Lehr, K. Katsaros, et al., "Revisiting wireless internet connectivity: 5G vs Wi-Fi6," *Telecommunications Policy*, Vol. 45, No. 5, 102127, 2021.
2. Sankaran, S. G. and S. R. Gulasekaran, *Wi-Fi6: Protocol and Network*, Artech House, 2021.
3. Naik, G., J.-M. Park, J. Ashdown, and W. Lehr, "Next generation Wi-Fi and 5G NR-U in the 6 GHz bands: Opportunities and challenges," *IEEE Access*, Vol. 8, 153027–153056, 2020.
4. Sun, J. X., Z. X. Huang, X. L. Wu, et al., "Design of image-reject hairpin filter applied for Ku-band LNB," *Proceedings of the 9th International Symposium on Antennas, Propagation and EM Theory*, 1161–1164, Guangzhou, 2010.
5. Yang, L., J. Qiang, S. Liu, et al., "A novel wideband bandpass filter based on CSRR-loaded substrate integrated folded waveguide," *International Journal of RF and Microwave Computer-aided Engineering*, Vol. 30, No. 6, e22181.1–e22181.9, 2020.
6. Vetry, R., A. S. Kochhar, and J. B. Shealy, "XBAW, an enabling technology for next generation resonators and filter solutions for 5G and Wi-Fi6/6E/7 applications (Invited)," *2022 International Electron Devices Meeting (IEDM)*, 6.1.1–16.1.4, 2022.
7. Tag, A., M. Schaefer, J. Sadhu, A. Tajic, et al., "Next generation of BAW: The new benchmark for RF acoustic technologies," *2022 IEEE International Ultrasonics Symposium (IUS)*, 1–4, 2022.
8. Luo, Z., A. Zhang, W. Huang, S. Shao, et al., "Aluminum nitride thin film based reconfigurable integrated photonic devices," *IEEE Journal of Selected Topics in Quantum Electronics*, Vol. 29, No. 3, 1–19, 2023.
9. Qamar, A. and M. Rais-Zadeh, "Coupled BAW/SAW resonators using AlN/Mo/Si and AlN/Mo/GaN layered structures," *IEEE Electron Device Letters*, Vol. 40, No. 2, 321–324, 2019.
10. Marín, S., J. D. Martínez, C. I. Valero, et al., "Microstrip filters with enhanced stopband based on lumped bisected pi-sections with parasitics," *IEEE Microwave and Wireless Components Letters*, Vol. 27, No. 1, 19–21, 2017.
11. Xiang, K. R. and F. C. Chen, "Compact microstrip bandpass filter with multispurious suppression using quarter-wavelength and half-wavelength uniform impedance resonators," *IEEE Access*, Vol. 6, 20364–20370, 2018.
12. Ali, N. O., M. R. Hamid, M. K. A. Rahim, et al., "A compact second-order chebyshev bandpass filter using U-shaped resonator and defected ground structure," *Radioengineering*, Vol. 29, No. 2, 321–327, 2020.
13. Liu, L. Q., P. Zhang, M. H. Weng, et al., "A miniaturized wideband bandpass filter using quarter-wavelength stepped-impedance resonators," *Electronics*, Vol. 8, No. 12, 1540, 2019.
14. Saleh, S., W. Ismail, M. H. Jamaluddin, et al., "5G hairpin bandpass filter," *Jordanian Journal of Computers and Information Technology (JJCIT)*, Vol. 7, No. 1, 1–12, 2021.
15. Wan, F., L. Wu, B. Ravelo, et al., "Analysis of interconnect line coupled with a radial-stub terminated negative group delay circuit," *IEEE Transactions on Electromagnetic Compatibility*, Vol. 62, No. 5, 1813–1821, 2020.